nature biotechnology

Guided self-organization and cortical plate formation in human brain organoids

Madeline A Lancaster[1,2], Nina S Corsini[1], Simone Wolfinger[1], E Hilary Gustafson[1], Alex W Phillips[2], Thomas R Burkard[1,3], Tomoki Otani[4], Frederick J Livesey[4] & Juergen A Knoblich[1]

Three-dimensional cell culture models have either relied on the self-organizing properties of mammalian cells[1–6] or used bioengineered constructs to arrange cells in an organ-like configuration[7,8]. While self-organizing organoids excel at recapitulating early developmental events, bioengineered constructs reproducibly generate desired tissue architectures. Here, we combine these two approaches to reproducibly generate human forebrain tissue while maintaining its self-organizing capacity. We use poly(lactide-co-glycolide) copolymer (PLGA) fiber microfilaments as a floating scaffold to generate elongated embryoid bodies. Microfilament-engineered cerebral organoids (enCORs) display enhanced neuroectoderm formation and improved cortical development. Furthermore, reconstitution of the basement membrane leads to characteristic cortical tissue architecture, including formation of a polarized cortical plate and radial units. Thus, enCORs model the distinctive radial organization of the cerebral cortex and allow for the study of neuronal migration. Our data demonstrate that combining 3D cell culture with bioengineering can increase reproducibility and improve tissue architecture.

Three-dimensional, self-organizing *in vitro* tissues called organoids have many potential applications in drug discovery and disease research. However, their utility has been limited by high variability, random tissue identity and incomplete morphological differentiation[9,10]. To identify sources of variability in brain organoids[11], we examined multiple independent batches of organoids at various stages. We found that while early organoids at the embryoid body stage were virtually indistinguishable from each other (**Supplementary Fig. 1a**), variation, especially between batches, became apparent during neural induction. Seven independent batches of cerebral organoids

from three human pluripotent stem cell (hPSC) lines revealed variable efficiency of polarized neural ectoderm formation over a range of 30–100% of organoids per batch (**Supplementary Fig. 1b,c**), suggesting that inconsistent neural induction efficiency might be a main source of variability.

Because most brain organoid protocols start from spherical embryoid bodies[12–14], and the neuroectoderm develops on the exterior of the embryoid body, we hypothesized that high variability may be due to low surface-area-to-volume ratio. To test this hypothesis, we generated embryoid bodies of varying sizes by seeding different numbers of cells, from 100 to 9,000 cells, because smaller-sized spheres would have a larger surface-area-to-volume ratio. Indeed, the smaller embryoid bodies showed more relative clearing, indicative of neuroectoderm[15] (**Supplementary Fig. 1d**). Further staining for identity markers revealed a decrease in the amount of cells with non-neuroectodermal identity, such as mesoderm and endoderm, in smaller embryoid bodies (**Supplementary Fig. 1e**). Upon Matrigel embedding, the smaller embryoid bodies continued to show less non-neural tissues, suggesting this could represent a route to generation of more pure neural tissues (**Supplementary Fig. 1f**). However, the neuroepithelial buds were smaller, and there were fewer of them overall compared with those seen in larger embryoid bodies (**Supplementary Fig. 1g**). Furthermore, when embryoid bodies were generated with the smallest number of cells (100), a larger fraction of those embryoid bodies failed to progress to organoids. Therefore, we turned to alternative approaches to increase the surface-area-to-volume ratio while maintaining large tissues overall.

Recent studies have shown that pluripotency[16] and germ layer identity during differentiation[17] are influenced when PSCs are grown on micropatterned substrates. However, this approach is incompatible with current organoid protocols that require non-adhesion to a surface and extensive cell–cell contact for self-organization. We therefore sought to physically micropattern, or guide, three-dimensional (3D) differentiation by using a floating scaffold[18] to shape the organoids at the embryoid body stage from the inside. To limit cell–scaffold contact we tested a protocol using micrometer-scale individual filaments that would contact only the innermost layer of cells of the embryoid body (**Fig. 1a**). We reasoned that this would allow for the formation of large

tissues with greater surface-area-to-volume ratio while maintaining dense cell–cell contact and self-organization.

Filaments were obtained from braided fibers of PLGA-10:90 by mechanical dispersion (**Supplementary Fig. 2a–c**). This bio-compat-

ible material is hydrolyzed in living tissue within 8–10 weeks[19]. 5–10 microfilaments were collected in a random configuration at the bottom of a low-attachment round-bottom microwell and seeded with 18,000 hPSCs, a ratio where only 5–10% of cells directly contact the
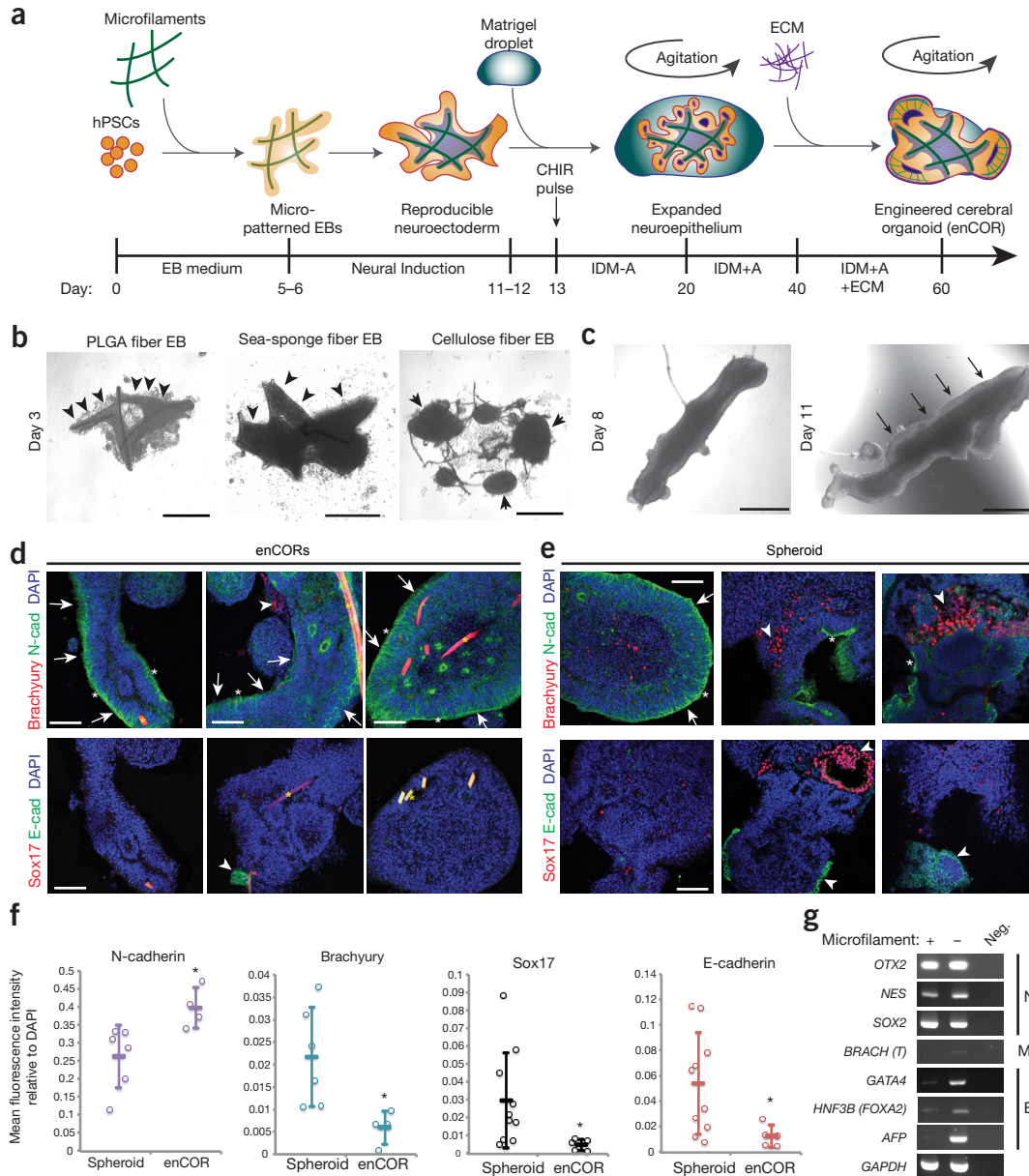
Figure 1 Engineered cerebral organoids reproducibly generate elongated neuroepithelium. (**a**) Schematic of the method for generating engineered cerebral organoids (enCORs). Timeline and media used are shown at the bottom. Specific timing should be tailored to the developing morphology of the tissue, as detailed in Online Methods. (**b**) hPSCs attach to and coat the PLGA microfilaments (left panel, arrowheads) as well as fibers derived from sea sponge (middle panel), whereas cellulose fibers with similar dimensions (right panel) fail to form elongated embryoid bodies at day 3 with H9 cells, and instead remain as clumps (arrows) only partially attached to the fibers. (**c**) Bioengineered embryoid bodies from H9 cells at two time points, days 8 and 11, during neural induction, showing clearing along the edges and polarized neural ectoderm (arrows). (**d**) Immunohistochemical staining of day-10 bioengineered H9 embryoid bodies for the germ layer markers Brachyury for mesoderm, N-cadherin for neural ectoderm, Sox17 for endoderm, and E-cadherin for non-neural epithelium. Note the prevalence of polarized neural epithelia (arrows) displaying the apical domain on the surface (white asterisks) with only occasional other germ layer identities (arrowhead). The microfilament can be seen as an autofluorescent rod (yellow asterisks). (**e**) Immunohistochemical staining of day-10 H9 spheroids for the same germ layer markers. Again, note the polarized neural epithelia (arrows) displaying the apical domain on the surface (white asterisks) on an optimal brain organoid (upper left panel), while extensive mesoderm and endoderm identities (arrowheads) are visible in suboptimal organoids. (**f**) Quantification of fluorescence staining of the above markers (mean gray value relative to DAPI). Dot-plot, mean ± s.d. *$P < 0.05$, Student's two-tailed t-test, $n = 6$–10 spheroids (10 d, H9), $n = 4$ enCOR organoids (10 d, H9). (**g**) RT-PCR for expression of markers of the three germ layers: neuroectoderm (NE), mesoderm (ME), and endoderm (EN) in 20-d microfilament organoids and organoids lacking a filament (spherical organoids), both made from H9 cells. Neg. is the negative water control. Images are cropped from full-length gels shown in **Supplementary Figure 3b**. Scale bars: 500 mm in **b**, 250 mm in **c**, 100 mm in **d,e**.

filament. The hPSCs attached evenly along the length of PLGA microfilaments (**Fig. 1b** and **Supplementary Fig. 2d**) or an alternative material, sea-sponge-derived fibers composed of the collagen-type protein spongin (**Fig. 1b** and **Supplementary Fig. 2e**). Embryoid bodies generated with cellulose microfilaments (**Supplementary Fig. 2f**) resulted in round aggregates only partially attached to the fibers (**Fig. 1b**). Thus, the choice of filament material is important for adherence of cells along the entire length. We pursued PLGA microfilaments further due to their availability and ease of obtaining sterile fibers.

The resulting enCORs displayed elongated morphologies but maintained typical dense cell composition. Like spherical embryoid bodies, they progressively grew in size and exhibited clearing along the edges, eventually forming polarized neural ectoderm. However, the neural ectoderm was elongated (**Fig. 1c**), and the efficiency of neuroectoderm formation was much improved, with consistent neural induction in all of seven independent preparations examined (**Supplementary Fig. 2g–i**).

Staining of early-stage microfilament-engineered embryoid bodies for germ layer markers revealed consistent generation of polarized neuroepithelium with concomitantly decreased amounts of endoderm and mesoderm identities (**Fig. 1d**). This was in contrast with spherical organoids, which often displayed non-ectodermal identities, especially in suboptimal organoids (**Fig. 1e**). Quantification of these identities demonstrated the reproducible formation of neuroectoderm in enCORs with an almost complete lack of non-neural tissues, whereas spheroids displayed highly variable amounts of all germ layer identities (**Fig. 1f**). Furthermore, expression analysis of pluripotency and germ layer markers by RT-PCR revealed a decrease in non-neural identities in enCOR organoids (**Fig. 1g** and **Supplementary Fig. 3a,b**). As organoids developed, enCORs displayed fewer morphological features of these other identities, such as the formation of early fluid-filled cysts (**Supplementary Fig. 3c**). Furthermore, enCORs contained large lobes of brain tissue but only a few regions expressing
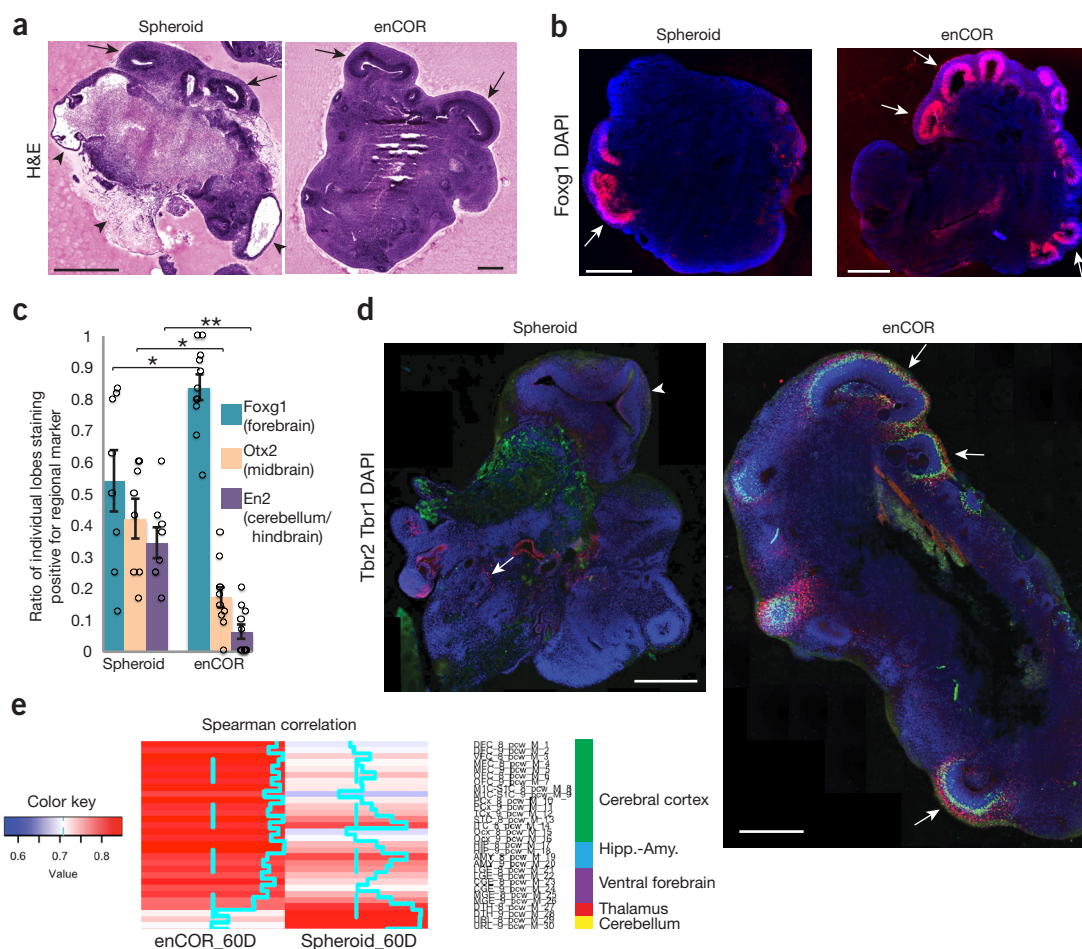

Figure 2 enCORs show increased forebrain identity. (**a**) H&E staining of representative 40-day spherical and enCOR organoids from H9 cells. Spheroids contain lobes of brain tissue (arrows) but also non-neural regions such as fluid-filled cysts and fibrous regions (arrowheads). enCORs instead contain pure neural tissue and many large continuous lobes of brain tissue (arrows). (**b**) Representative sections of whole 40-d H9 organoids stained for the forebrain marker Foxg1. enCORs display more Foxg1^{+} lobes (arrows) compared with spheroids. (**c**) Quantification of the mean ratio of individual lobes displaying positive staining for the specified regional markers (see **Supplementary Fig. 4e** for representative stained sections). Foxg1^{+} regions represent forebrain, regions highly positive for Otx2 represent midbrain, En2^{+} regions represent cerebellar or hindbrain identities. Error bars are s.e.m. *$P < 0.01$, **$P < 0.0001$, Student's two-tailed t-test, $n = 8$ spheroids (40 d, H9) from three independent batches, $n = 11$ enCOR organoids (40 d, H9) from four independent batches. (**d**) Staining of day 40 H9 enCOR brain organoids and spheroids for the markers of dorsal cortex Tbr1 and Tbr2 reveals large lobes of tissue that are dorsal cortex (arrows) in enCORs. Spheroids show many fewer dorsal regions and some large brain regions that lack this identity (arrowhead). (**e**) Heatmap of Spearman correlation coefficients of differentially expressed genes at 60 d in H9 spheroids and enCORs with the Allen BrainSpan transcriptome[22]. All brain regions are shown for stage I (8–9 post-conception weeks, see **Supplementary Fig. 7c**), sorted by anterior-posterior regional identity. Hipp.-Amy.: Hippocampus – Amygdala. Scale bars: 500 mm in **a,b,d**.
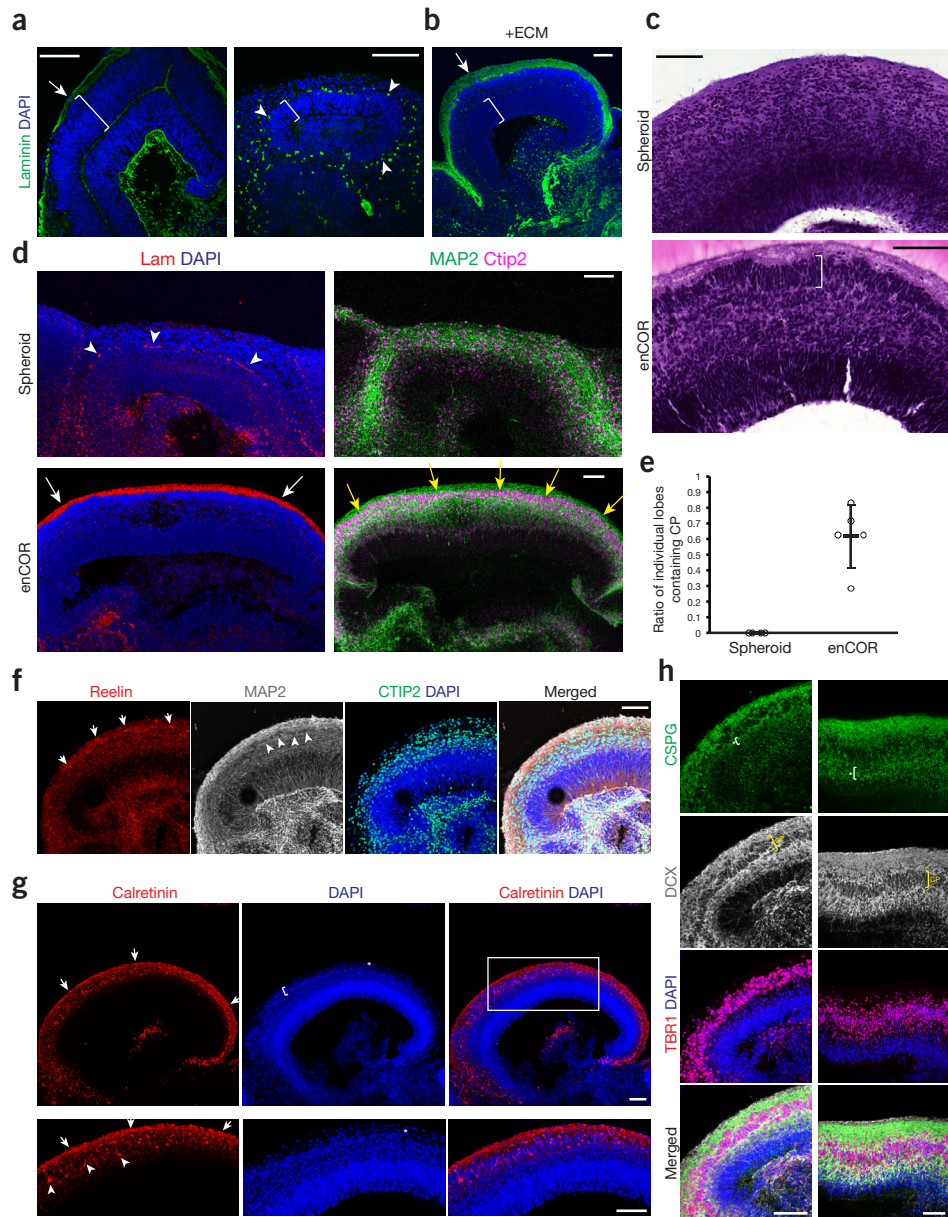
Figure 3 enCORs with reconstituted basement membrane form cortical plate. (**a**) Staining for the basement membrane component laminin (green) in a day-48 H9 spheroid. Note the presence of the basement membrane surrounding a region of early neuroepithelium before the generation of neurons (left panel, arrow), whereas another, more developed region displays neuron generation and only sparse laminin labeling remains (right panel, arrowheads) adjacent to the ventricular zone (VZ, brackets) rather than over the surface of the organoid. (**b**) Laminin staining of a 60-d H9 enCOR following treatment with dissolved extracellular matrix (ECM) in the form of Matrigel. Note the presence of a laminin-rich basement membrane covering the surface of the organoid (arrow) and outside both the VZ (bracket) and newly generated neurons. (**c**) Histological staining by H&E reveals the presence of a radially oriented dense CP (lower panel, bracket) in enCORs with ECM, in contrast to the disorganized neurons of a spheroid (upper panel). Both are 60-d H9-derived organoids. (**d**) Immunohistochemical staining for laminin and the neuronal markers MAP2 and Ctip2 in day-60 H9 spheroid and enCOR organoids. Note the presence of remnant basement membrane in the spheroid (arrowheads), whereas in the enCOR with ECM a basement membrane (white arrows) forms outside the dense Ctip2+ cortical plate (yellow arrows). (**e**) Quantification of the mean ratio of individual lobes displaying a CP in H&E-stained sections of day-60 H9 organoids. Individual lobes were identified by the presence of a ventricular space and radial VZ. CP was identified by the presence of a condensed band separated from the VZ by a cell-sparse zone. Each point is an independent batch of 2 or 3 organoids, each with several lobes of brain tissue. $n = 4$ independent batches of 12 spheroids, $n = 5$ independent batches of 12 enCORs. Mean across batches shown ± s.d. (**f**) Staining for reelin in a dorsal cortical region early in CP formation (day-56 H9 enCOR). Several cells, which are strongly reactive for reelin (arrows), localize outside the newly forming CP (arrowheads, recognizable by the lower intensity Map2 staining), consistent with Cajal–Retzius identity. Staining can also be seen more diffusely, consistent with its secreted role. (**g**) Staining for calretinin, another marker of Cajal–Retzius cells, in a day-53 H9 enCOR, labels cells outside (left panels, arrows) the newly forming CP. Note the gradient of CP formation with more advanced CP to the left (visible in middle panels, bracket), and the initiation to the right (asterisk). (Inset is enlarged in lower panels.) Where the CP is further developed, one can also observe calretinin+ cells internal (arrowheads) to the CP, consistent with preplate splitting and interneuron identity. (**h**) Staining for chondroitin sulfate proteoglycan (CSPG) in day-68 H9 enCORs further demonstrates preplate splitting. Panels on the left show a less developed CP (yellow brackets) with the initiation of splitting and SP formation (white brackets with asterisk), while panels on the right show a more developed CP with layers consistent with SP, CP, and MZ. DCX, neuronal marker Doublecortin. Scale bars: 100 mm in all panels.

markers for endoderm and non-neural epithelia (**Supplementary Fig. 3d**), in contrast to spherical organoids. Thus, enCORs displayed more reproducible neural induction without sacrificing self-organization.

We observed that the neuroepithelial buds that formed upon Matrigel embedding were less elongated and continuous in organoids with micro-filaments (**Supplementary Fig. 4a**). Because Wnt pathway activation has been shown to induce lateral expansion of cortical neuroepithelium[20], we applied the GSK3beta inhibitor/Wnt activator CHIR99021 (CHIR) after neuroepithelial budding. This treatment resulted in larger lumens with surrounding continuous neuroepithelium (**Supplementary Fig. 4b**). Because Wnt signaling is also an important patterning factor[21], and we sought to limit the extent of exogenous patterning, we performed treatment for only a short 3-d pulse. This treatment alone did not influence germ layer induction or overall organoid morphology (**Supplementary Fig. 4c,d**).

The combination of microfilament and CHIR pulse resulted in more consistent formation of brain lobules (**Fig. 2a**) that were large, compared with spheroids, and that stained positive for the forebrain marker Foxg1 (**Fig. 2b**). In addition, we observed reduced frequency of Otx2+ mid-brain and En2+ cerebellar/hindbrain regions (**Supplementary Fig. 4e**). Quantification of these identities revealed more reproducible formation of forebrain, rather than other brain regions, in enCORs (**Fig. 2c**). Consistent with this, enCORs displayed both dorsal and ventral forebrain regions (**Supplementary Fig. 4f**) with more frequent large Tbr1- and Tbr2-positive dorsal cortical regions (**Fig. 2d**). Furthermore, enCORs displayed regions consistent with choroid plexus and hippocampus identity (**Supplementary Fig. 4g,h**). Thus, together with late GSK3beta inhibition, bioengineering of cerebral organoids results in reproducible formation of forebrain tissue with little contamination from other germ layers and brain regions.

To further examine the effect of the microfilament and CHIR addition, we analyzed gene expression by RNA-seq at 20 and 60 d in three enCORs compared with three spherical organoids (**Supplementary Table 1**). 20-d-old enCORs were enriched for the Gene Ontology (GO) terms "neurological system process" and "multicellular organismal process," while other organ development terms, such as "digestive tract mesoderm development," "muscle organ development," "skeletal system development," and "mesoderm development," were decreased compared with spheroids (**Supplementary Fig. 5a**). At 60 d, we observed GO term enrichment for "nervous system development" and terms associated with transcription, while "digestive tract mesoderm development," "heart development," muscle and skeletal system terms, and "synaptic transmission" were decreased. The decrease in synaptic genes at 60 d suggests a delay in neuronal maturation, perhaps due to extended progenitor expansion upon CHIR addition. Hierarchical clustering revealed several gene clusters displaying specific patterns of differential expression (**Supplementary Figs. 5b** and **6** and **Supplementary Table 2**). Cluster 1 was upregulated in 60-d enCORs and enriched for forebrain and cortical differentiation. Clusters 4 and 5 were increased or unchanged at 20 d but decreased at 60 d and were enriched for nervous system development and synaptic transmission. Clusters 6 and 7 were decreased at 20 d and also decreased or unchanged at 60 d. They were enriched for more caudal expression, such as spinal cord and hindbrain, consistent with the effect of bioengineering and CHIR addition on forebrain patterning.

We next assessed expression of specific germ layer or brain patterning markers (**Supplementary Fig. 7a,b**). The pluripotency markers Oct4, Klf4, and Nanog were decreased in enCORs. Neuroectodermal markers appeared unchanged whereas mesendodermal markers such as Sox17, T (Brachyury), Mixl1, and Foxa2 were decreased. Furthermore, the forebrain marker Foxg1 was sharply increased, whereas caudal markers such as En2, Gbx2, and Hox genes were decreased. Finally, dorsal forebrain

markers such as Emx1, Tbr1, and Tbr2 were increased, while ventral forebrain markers were unchanged. These findings suggest a more rostral brain identity in enCORs.

Finally, we compared genes differentially expressed between 60-d spherical organoids and enCORs to gene expression in the human developing brain using the Allen BrainSpan Atlas[22] (**Supplementary Fig. 7c**). enCORs most closely matched the forebrain identities of the human brain at early gestation, specifically 8–9 weeks post-conception (**Fig. 2e**). Spherical organoid gene expression instead had the highest correlation with that of more caudal regions at this time, specifically the thalamus and cerebellum, and, at later time points, showed a broader correlation with other brain regions (**Supplementary Fig. 7c**). These findings are consistent with the effect of the microfilament and CHIR addition on forebrain regional identity.

Neurons in the developing cortex *in vivo* form a dense band called the cortical plate (CP) and show radially aligned morphology. This is thought to reflect their organization into radial units[23], a prerequisite for the formation of functional neuronal columns in the adult cortex[24,25]. Although *in vitro* models, including organoids, properly recapitulate basal translocation of neurons and even formation of rudimentary layers reminiscent of the CP[26–28], radially aligned neurons in a dense CP have not been observed, nor have radial units. This might be due to the absence of a basement membrane, which is thought to be generated by the overlying non-neural mesenchyme[29,30] not present in organoids. Indeed, although staining for laminin initially revealed a well-formed basement membrane in early neuroepithelium before neurogenesis, this changed to dispersed, punctate staining, suggesting breakdown and/or failure to maintain the membrane upon generation and basal migration of neurons (**Fig. 3a**).

To reconstitute the basement membrane, we tested exogenous extra-cellular matrix (ECM) components in the form of dissolved Matrigel in the media. Indeed, this treatment maintained a thick laminin-rich basement membrane that remained outside the migrating neurons (**Fig. 3b**). Brightfield imaging revealed a band of density in cortical regions that was absent in organoids lacking dissolved ECM (**Supplementary Fig. 8a**). Subsequent sectioning and histological staining revealed a radialized basal layer consistent with cortical plate morphology (**Fig. 3c**). Indeed, immunohistochemical staining revealed it was positive for the neural markers Ctip2 and Map2, with a band of lower intensity Map2 staining in cell bodies that is typical of the cortical plate *in vivo* (**Fig. 3d** and **Supplementary Fig. 8b**). This treatment elicited CP formation in organoids from three independent cell lines: two human embryonic stem cell (hESC) lines and one induced pluripotent stem cell (iPSC) line (**Supplementary Fig. 8c**), and quantification of the presence of a CP revealed reproducible formation in five independent batches of enCORs while a CP was never observed in spheroids (**Fig. 3e**).

To examine the role of Matrigel and whether it is necessary for formation of a CP, we treated enCORs with the matrix metalloprotease inhibitor GM6001 to test whether inhibition of ECM breakdown is instead sufficient for CP formation. Continuous treatment beginning at day 30 did not result in CP formation by 60 d (**Supplementary Fig. 8d**), suggesting that it is not simply a breakdown of the initial basement membrane that inhibits CP formation in the spherical organoid method, but also a failure to maintain and expand the basement membrane with tissue growth, a hurdle overcome by addition of dissolved Matrigel. We next tested whether laminin alone, in combination with entactin, or the combination of laminin–entactin–collagen would be sufficient to recapitulate the effect of dissolved Matrigel. These treatments did not recapitulate the extent of CP formation seen with Matrigel (**Supplementary Fig. 8e**), suggesting other components of this complex ECM are important for basement membrane maintenance.
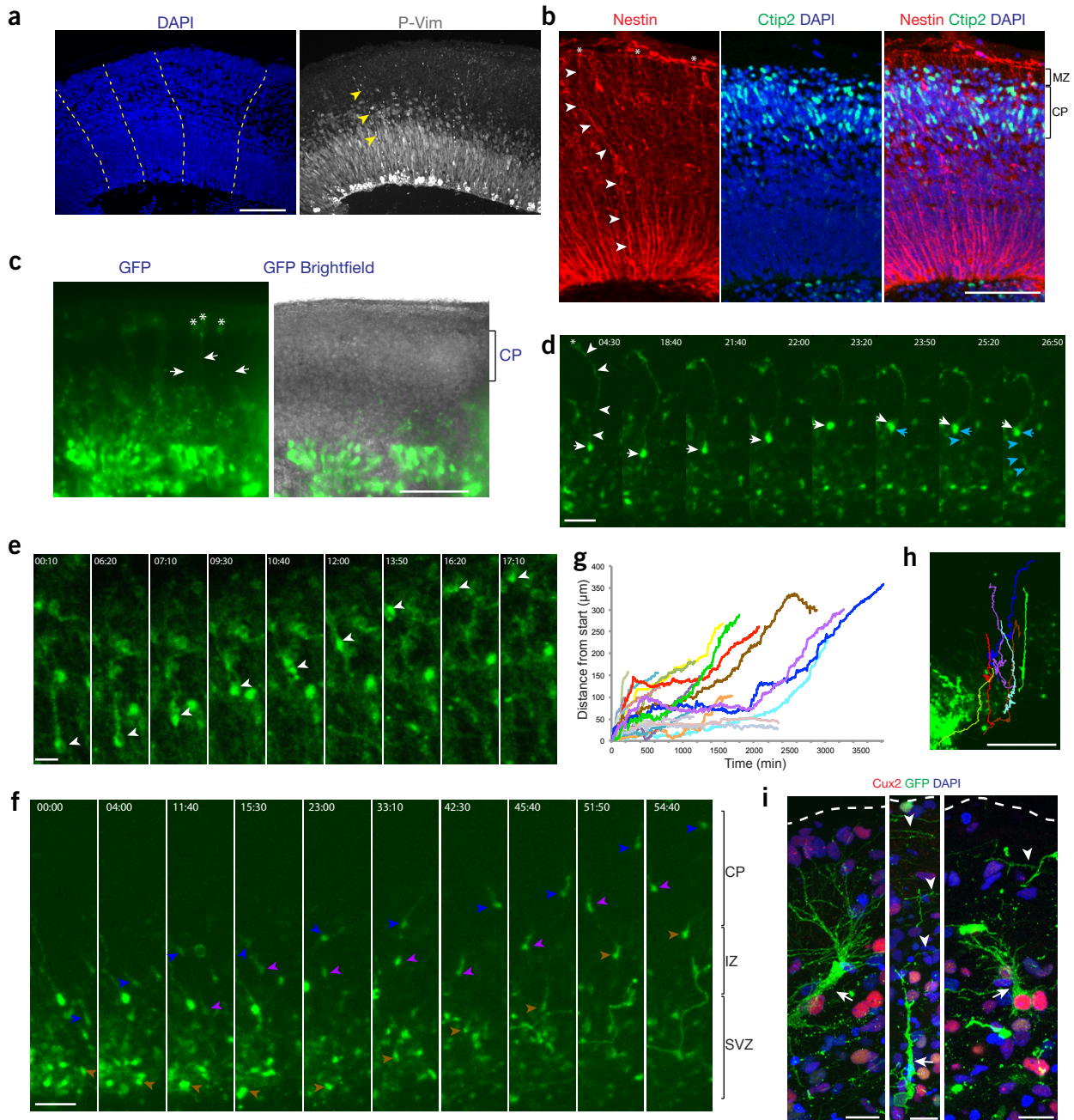
Figure 4 enCORs display radial units and radial neuronal migration. (**a**) Nuclear staining by DAPI in a 60-d H9 enCOR reveals radially organized units (dashed lines) while sparse staining for radial glial fibers with the marker of mitotic radial glia phosphorylated vimentin reveals fibers that extend the width of the tissue (arrowheads) reminiscent of a radial scaffold. (**b**) Nestin staining for radial glia in day-70 H1 enCORs reveals long basal processes (arrowheads) that terminate with end-feet at the surface of the organoid (asterisks) outside the CP and MZ. (**c**) Electroporation of the VZ of a 64-d H9 enCOR with a GFP construct and vibratome sectioning the next day reveals individual RG basal processes (arrows) that extend to the outer surface (asterisks). (**d**) Frames from live imaging of an outer/basal RG (arrow marks the cell body) in a H1 enCOR electroporated with GFP on day 63, followed by vibratome sectioning 4 d later and live imaging 24 h later (**Supplementary Video 1**). Note the long basal process (arrowheads) and end-foot (asterisk) as well as a division event including mitotic somal translocation beginning at 21:40. The newly generated daughter cell (blue arrow) then extends a process apically (blue arrowheads). Time stamp is hours:minutes. (**e**) Frames from live imaging (**Supplementary Video 5**) of a membrane targeted farnesyl-GFP-labeled neuron (arrowhead), showing radial migration into the CP. Time stamp is hours:minutes. (**f**) Live imaging of migration of several neurons (arrowheads) in the same sample as **d**, displaying typical radial migration including transient stalling with multipolar morphology (e.g., blue arrowhead 11:40 to 23:00). Stills taken from **Supplementary Video 1**. Colors of the arrowheads match traces shown in **g** and **h**. Time stamp is hours:minutes. SVZ, subventricular zone; IZ, intermediate zone. (**g**) Traces of distance traveled of 22 individual neurons from **Supplementary Videos 1**, **2**, and **4**. Colors of the traces match those shown in **h**. Note the characteristic transient stalling in several of the traces (red, blue, purple) with shorter duration stalling in the green and brown traces, while the light blue trace is already stalled at the start of the movie. (**h**) Movement traces of individual neurons quantified in **g** and seen in **f**, showing the movement into the intermediate zone with stalling and subsequent movement into the CP. (**i**) Individual neurons labeled by electroporation of an H9 enCOR at day 64 with an integrating farnesylated GFP construct to allow for long-term labeling and analysis after 36 d. Note the primary dendrite extending from the cell body (arrows) toward the outer surface (dashed lines), as well as many parallel fibers (arrowheads) in the outer MZ. Scale bars: 100 mm in **a,b,c,h**; 50 mm in **d,f**; 20 mm in **e,i**.

Recently, SFEBq forebrain organoids were combined with several modifications, including dissolved Matrigel in the media, which leads to condensation of neurons superficial to progenitor zones, reflecting an organization reminiscent of CP formation[26]. Furthermore, forebrain organoids and so-called cortical spheroids have both been described to exhibit features of cortical layers[27,28], an organization that *in vivo* depends upon proper CP formation. We therefore compared the enCOR method with these previous approaches to specifically test CP formation. While the SFEBq method[26] produced occasional somewhat condensed cells reminiscent of a CP, neither SFEBq organoids nor cortical spheroids displayed a clear, radially organized CP as seen in enCORs (**Supplementary Fig. 9a,b**). These data suggest that while cortical layering may occur to some extent in the earlier methods, in enCORs the events leading to proper neuronal organization may be more similar to *in vivo* development.

CP establishment *in vivo* depends upon early pioneer neurons of the preplate, which secrete reelin to attract subsequent neurons to migrate into and split the preplate into the marginal zone (MZ) and subplate (SP). We therefore tested whether enCORs exhibited Reelin-expressing neurons, also called Cajal–Retzius cells, by staining for reelin and calretinin. Staining for reelin revealed strongly reactive cells in the most superficial regions, as well as more dispersed signal indicative of the fact that reelin is a secreted factor (**Fig. 3f**). Furthermore, calretinin staining revealed neurons in superficial regions as well as just inside the newly forming CP (**Fig. 3g**), a pattern typical of preplate splitting *in vivo*. Staining for chondroitin sulfate proteoglycan further revealed splitting and establishment of MZ and SP during early CP condensation (**Fig. 3h**). This separation was more pronounced with more developed, thicker CP. Furthermore, the CP itself widened over time and even displayed features of early cortical layering (**Supplementary Fig. 9c**).

The basal process of radial glial cells, which contacts the basement membrane covering the surface of the brain, acts as a scaffold for migration and orientation of neurons to allow for formation of the CP and positioning into radial units[31]. Nuclear staining in cortical regions of enCORs that had been sectioned evenly along the plane perpendicular to the apicobasal axis revealed linear units of radial glia and neurons aligned in a manner reminiscent of radial units (**Fig. 4a**), a characteristic architecture not previously recapitulated *in vitro*. Furthermore, staining for phospho-vimentin, a cytoplasmic marker of dividing radial glia revealed long basal processes extending the length of the cortical wall. These basal processes were also evident upon staining for nestin, a cytoplasmic marker of radial glia, which revealed processes with end feet that terminated on the outer surface (**Fig. 4b** and **Supplementary Fig. 10a**). In contrast, spherical organoids displayed disorganized radial glial processes with terminating end-feet at various locations within the tissue (**Supplementary Fig. 10b**).

In order to label individual cells for live imaging and morphological analyses, we next established combined electroporation and slice culture in organoids. We electroporated a GFP construct into the VZ of individual cortical lobes, sectioned the organoid by vibratome and cultured the slices at the air-liquid interface. This allowed for marking individual radial glia, further demonstrating the long basal processes terminating superficial to the CP (**Fig. 4c**).

Long-term live imaging of electroporated slices revealed various cell behaviors, including divisions of outer radial glia (oRG), also called basal radial glia (**Fig. 4d** and **Supplementary Video 1**), which displayed mitotic somal translocation, a feature typical of oRGs *in vivo*[32]. Furthermore, live imaging of labeled newly generated neurons revealed typical radial migration into the intermediate zone and transient acquisition of multipolar morphology (**Supplementary Fig. 10c** and **Supplementary Videos 2** and **3**) before reestablishment of radial orientation and migration into the CP (**Fig. 4e,f** and **Supplementary Videos 1,4** and **5**). Tracing of 22 individual neurons from three independent experiments further highlighted the saltatory nature of their radial migration, with long stationary periods in the intermediate zone (**Fig. 4g,h**). Finally, we could also observe migration of putative interneurons showing tangential movement and often more than one leading process that the cell moved between (**Supplementary Fig. 10d** and **Supplementary Videos 2** and **6**), a feature described for tangentially migrating interneurons *in vivo*[33]. Establishment of labeling and long-term live imaging of slice cultures in this manner thus provides a useful tool for examination of neuronal migration and progenitor division in a human model system.

Electroporation of a membrane-targeted GFP allowed for examination of morphology of single neurons in more-developed organoids. This revealed complex dendritic morphologies and neurons with a primary dendrite typical of the pyramidal morphology of cortical neurons (**Fig. 4i**). Furthermore, these neurons were oriented toward the MZ on the outer surface of the organoid where parallel fibers could frequently be seen. Finally, we performed calcium staining and live imaging on slice cultures, which revealed spontaneous calcium surges suggestive of neuronal activity (**Supplementary Fig. 10e** and **Supplementary Video 7**). These data point to proper positioning and maturation of cortical neurons in enCORs.

The remarkable self-organization and ability to generate the full repertoire of organ cell types have made organoids an important new model system. However, the high variability and difficulties modeling later tissue architecture has meant that subtle defects are difficult to discern. To overcome this, we tested two routes to increase the surface-area-to-volume ratio: 1) decreasing embryoid body size, and 2) bioengineering using a microscale internal scaffold. Each approach could have interesting future applications. Smaller embryoid bodies may be a good route to higher-throughput analysis and drug testing, while the scaffold allows for larger, continuous cortical lobes and opens the door to future development, such as testing of alternative materials, adsorption of instructive factors, and even gradient generation for axis formation. Overall, we show that increasing surface area leads to reproducible neural induction, and the combination of bioengineering and self-organization allows for reliable forebrain formation without sacrificing tissue complexity. Importantly, there are still noticeable differences between different cell lines and batches, for example, in terms of tailoring the timing needed for each step. However, because enCORs show more reliable generation of forebrain and proper migration and formation of a CP, the number of potentially discernable phenotypes is greatly increased. Furthermore, the application of slice culture and live imaging to brain organoids allows for the study of dynamic processes in cortical development, including progenitor division and migration.

Note: Any Supplementary Information and Source Data files are available in the online version of the paper.

METHODS

Methods, including statements of data availability and any associated accession codes and references, are available in the online version of the paper.

AUTHOR CONTRIBUTIONS

COMPETING FINANCIAL INTERESTS

1. Rookmaaker, M.B., Schutgens, F., Verhaar, M.C. & Clevers, H. Development and application of human adult stem or progenitor cell organoids. *Nat. Rev. Nephrol.* **11**, 546–554 (2015).
2. Fatehullah, A., Tan, S.H. & Barker, N. Organoids as an *in vitro* model of human development and disease. *Nat. Cell Biol.* **18**, 246–254 (2016).
3. Yin, X. *et al.* Engineering stem cell organoids. *Cell Stem Cell* **18**, 25–38 (2016).
4. Dedhia, P.H., Bertaux-Skeirik, N., Zavros, Y. & Spence, J.R. Organoid models of human gastrointestinal development and disease. *Gastroenterology* **150**, 1098–1112 (2016).
5. Sasai, Y. Next-generation regenerative medicine: organogenesis from stem cells in 3D culture. *Cell Stem Cell* **12**, 520–530 (2013).
6. Lancaster, M.A. & Knoblich, J.A. Organogenesis in a dish: modeling development and disease using organoid technologies. *Science* **345**, 1247125–1247125 (2014).
7. Langer, R. & Vacanti, J. Advances in tissue engineering. *J. Pediatr. Surg.* **51**, 8–12 (2016).
8. Esch, E.W., Bahinski, A. & Huh, D. Organs-on-chips at the frontiers of drug discovery. *Nat. Rev. Drug Discov.* **14**, 248–260 (2015).
9. Xinaris, C., Brizi, V. & Remuzzi, G. Organoid models and applications in biomedical research. *Nephron* **130**, 191–199 (2015).
10. Hynds, R.E. & Giangreco, A. Concise review: the relevance of human stem cell-derived organoid models for epithelial translational medicine. *Stem Cells* **31**, 417–422 (2013).
11. Lancaster, M.A. & Knoblich, J.A. Generation of cerebral organoids from human pluripotent stem cells. *Nat. Protoc.* **9**, 2329–2340 (2014).
12. Eiraku, M. *et al.* Self-organized formation of polarized cortical tissues from ESCs and its active manipulation by extrinsic signals. *Cell Stem Cell* **3**, 519–532 (2008).
13. Mariani, J. *et al.* Modeling human cortical development *in vitro* using induced pluripotent stem cells. *Proc. Natl. Acad. Sci. USA* **109**, 12770–12775 (2012).
14. Lancaster, M.A. *et al.* Cerebral organoids model human brain development and microcephaly. *Nature* **501**, 373–379 (2013).
15. Eiraku, M. *et al.* Self-organizing optic-cup morphogenesis in three-dimensional culture. *Nature* **472**, 51–56 (2011).
16. Caiazzo, M. *et al.* Defined three-dimensional microenvironments boost induction of pluripotency. *Nat. Mater.* **15**, 344–352 (2016).
17. Warmflash, A., Sorre, B., Etoc, F., Siggia, E.D. & Brivanlou, A.H. A method to recapitulate early embryonic spatial patterning in human embryonic stem cells. *Nat. Methods* **11**, 847–854 (2014).
18. Oh, S.K.W. *et al.* Long-term microcarrier suspension cultures of human embryonic stem cells. *Stem Cell Res. (Amst.)* **2**, 219–230 (2009).
19. Molander, H., Olsson, Y., Engkvist, O., Bowald, S. & Eriksson, I. Regeneration of peripheral nerve through a polyglactin tube. *Muscle Nerve* **5**, 54–57 (1982).
20. Chenn, A. & Walsh, C.A. Regulation of cerebral cortical size by control of cell cycle exit in neural precursors. *Science* **297**, 365–369 (2002).
21. Subramanian, L., Remedios, R., Shetty, A. & Tole, S. Signals from the edges: the cortical hem and antihem in telencephalic development. *Semin. Cell Dev. Biol.* **20**, 712–718 (2009).
22. Miller, J.A. *et al.* Transcriptional landscape of the prenatal human brain. *Nature* **508**, 199–206 (2014).
23. Rakic, P. Specification of cerebral cortical areas. *Science* **241**, 170–176 (1988).
24. Jones, E.G. & Rakic, P. Radial columns in cortical architecture: it is the composition that counts. *Cereb. Cortex* **20**, 2261–2264 (2010).
25. Geschwind, D.H. & Rakic, P. Cortical evolution: judge the brain by its cover. *Neuron* **80**, 633–647 (2013).
26. Kadoshima, T. *et al.* Self-organization of axial polarity, inside-out layer pattern, and species-specific progenitor dynamics in human ES cell-derived neocortex. *Proc. Natl. Acad. Sci. USA* **110**, 20284–20289 (2013).
27. Paşca, A.M. *et al.* Functional cortical neurons and astrocytes from human pluripotent stem cells in 3D culture. *Nat. Methods* **12**, 671–678 (2015).
28. Qian, X. *et al.* Brain-region-specific organoids using mini-bioreactors for modeling ZIKV exposure. *Cell* **165**, 1238–1254 (2016).
29. Sievers, J., Pehlemann, F.W., Gude, S. & Berry, M. Meningeal cells organize the superficial glia limitans of the cerebellum and produce components of both the interstitial matrix and the basement membrane. *J. Neurocytol.* **23**, 135–149 (1994).
30. Halfter, W., Dong, S., Yip, Y.-P., Willem, M. & Mayer, U. A critical function of the pial basement membrane in cortical histogenesis. *J. Neurosci.* **22**, 6029–6040 (2002).
31. Rakic, P. Evolution of the neocortex: a perspective from developmental biology. *Nat. Rev. Neurosci.* **10**, 724–735 (2009).
32. Wang, X., Tsai, J.-W., LaMonica, B. & Kriegstein, A.R. A new subtype of progenitor cell in the mouse embryonic neocortex. *Nat. Neurosci.* **14**, 555–561 (2011).
33. Marín, O., Valiente, M., Ge, X. & Tsai, L.-H. Guiding neuronal cell migrations. *Cold Spring Harb. Perspect. Biol.* **2**, a001834 (2010).

ONLINE METHODS

Preparation of microfilaments. Poly (lactide-co-glycolide) braided fibers of PLGA-10:90 were obtained from a commercial source as Vicryl sutures (Ethicon, size 5-0). We preferentially used violet dyed fibers to assist in visualization during dispersion and within embryoid bodies. Individual microfilaments were isolated from the braided fiber by mechanical shearing with an angled blade against a stainless steel plate, to obtain filaments of 0.5–1 mm in length, and 15 μm in diameter. Filaments were then hydrated in embryoid body media and transferred to a 15-ml conical tube for storage at 4 °C. Filaments of cellulose were obtained by shaving individual fibers from a sheet of Whatman filter paper. Sea-sponge filaments were obtained by shaving fibers from a commercially available dried sea-sponge sample.

Preparation of embryoid bodies and enCORs. Spheroids were generated with 9,000 cells (unless stated otherwise) exactly as previously[14] except that typical quality control and elimination of suboptimal organoids[11] and batches were not performed in order to obtain the full spectrum of variability. Embryoid bodies were prepared from single-cell suspension following accutase treatment, as described previously[11]. Cell lines were human ES (H9 or H1, both from WiCell, and approved for use in this project by the UK Stem Cell Bank Steering Committee) or iPSCs (System Biosciences, SC101A-1), all of which have been authenticated by the provider and routinely tested for mycoplasma (with negative results)(MycoAlert, Lonza). Cells were counted and resuspended in embryoid body media: DMEM/F12 (Invitrogen, cat. #11330-032) and 20% Knockout Serum replacement (Invitrogen, cat. #10828-028), 3% human ESC quality batch-tested FBS, 1% Glutamax (Invitrogen, cat. #35050-038), 1% MEM-NEAA (Sigma, cat. #M7145), 0.1 mM 2-mercaptoethanol, 4 ng/ml bFGF (Peprotech, cat. #100-18B), and 50μM Y-27632 ROCK inhibitor (VWR, cat. #688000-5). For enCORs, 18,000 cells were added to each well of a 96-well low-attachment U-bottom plate (Sigma, cat. #CLS7007) already containing 5–10 microfilaments in embryoid body media, and media was added to give a final volume of 150 ml per well. Based on an average hPSC cell size of 15 mm (measured from hPSC cell suspensions on EVOS microscope, Invitrogen), we calculated that 18,000 cells per 5–10 fibers of maximum length 1 mm would result in, at most, 5–10% of cells having direct contact to the fiber.

At day 3, half of the media was replaced with embryoid body media without bFGF and Y-27632. On day 5 or 6, depending on morphology (when surface tissue exhibited signs of clearing as described previously[11]), embryoid bodies were moved with an angled cut P200 tip to obtain a wide bore opening to 24-well low-attachment plates (Sigma, cat. #CLS3473) with neural induction media (NI) as previously described[11]. Media was changed every other day. On day 11, or when polarized neural ectoderm was visible on the surface as shown in **Figure 1c**, enCORs were transferred to a droplet of Matrigel as previously described but kept in NI media. At day 13 (2 d after Matrigel embedding), media was changed to an improved differentiation media –A (IDM-A): 1:1 of DMEM/F12 and Neurobasal (Invitrogen, cat. #21103049), 0.5% N2 supplement (Invitrogen, cat. #17502048), 2% B27–vitamin A (Invitrogen, cat. #12587010), 0.25% insulin solution (Sigma, cat. #I9278-5ML), 50 μM 2-mercaptoethanol, 1% Glutamax, 0.5% MEM-NEAA, and 1% penicillin-streptomycin (Sigma, cat. #P0781). Additionally, CHIR 99021 (Tocris, cat. #4423) at 3 μM was added from day 13 to 16. Media was changed every other day and organoids were moved to an orbital shaker placed in the incubator, on days 18–20. After moving to the shaker, media was changed every 3–4 d. Importantly, shaking speed should be calculated based on the throw of the shaker. For a throw of 10 mm, speed should be 85 r.p.m. We noticed that an incorrect speed did not result in CP formation.

Formation of polarized cortical plate. At day 20, media was changed to an improved differentiation +A (IDM+A): 1:1 of DMEM/F12 and Neurobasal, 0.5% N2 supplement, 2% B27 +vitamin A, 0.25% insulin solution, 50 μM 2-mercaptoethanol, 1% Glutamax, 0.5% MEM-NEAA, 1% penicillin-streptomycin, 0.4 mM vitamin C, and 1.49 g HEPES per 500 ml to control pH levels. Alternatively, media can be pH-controlled with further bicarbonate buffering with the addition of 1 mg/ml sodium bicarbonate. At day 40, media was changed to IDM+A with 1 ml dissolved Matrigel per 50 ml media by slowly thawing the Matrigel on ice and adding to cold media to dissolve. For treatment with matrix metalloprotease inhibitor GM6001 (Selleck Chemicals S7157), a final concentration of 3 μM was added beginning on day 30. For testing purified ECM components, 35 μg/

ml of pure laminin (Corning 354232) was added beginning on day 40, or 45 ml of high concentration laminin/entactin gel (Corning 354259) was dissolved per 5 ml media, or a 70% laminin/entactin—30% Collagen I (Corning 354249) mixture (35 μl laminin/entactin + 25 μl collagen) was added to obtain a protein concentration comparable to final concentration of Matrigel as obtained above. For these treatments, organoids were allocated randomly to separate dishes containing the various components.

Cortical spheroids were generated as described previously[27]. Briefly, H9 feeder-free cells were dissociated with EDTA and intact colonies were plated in a low-attachment 6-cm dish in hESC media containing small molecules as detailed in the published protocol. On day 6, media was changed to Neural Media and addition of growth factors was performed with the timing described in the protocol. Forebrain SFEBq organoids were generated as previously[26] and as in Otani *et al.*[34]. Briefly, iPSCs were dissociated to single cells and 9,000 cells plated per low attachment u-bottom well in cortex differentiation media containing small molecules as described in the published protocol. Media changes were performed as described and on day 19 the tissues were moved to DMEM/F12 +N2-based media with subsequent addition of FBS, heparin and Matrigel on day 35 as described. B27 was included starting at day 70, along with increased Matrigel exactly as described.

Histological and immunohistochemical analysis. Organoids were fixed in 4% paraformaldehyde for 20 min at room temperature and washed with PBS three times for 10 min each at room temperature before allowing to sink in 30% sucrose at 4 °C. The tissues were embedded and sectioned and stained as described[11]. Primary antibodies used were: goat anti-Brachyury (R&D Systems AF2085, 1:200), mouse anti-N-cadherin (BD 610920, 1:500), mouse anti-E-cadherin (BD 610182, 1:200), goat anti-Sox17 (R&D systems AF1924, 1:200), rabbit anti-laminin (Sigma L9393, 1:500), rabbit anti-Tbr1 (Abcam ab31940, 1:300), chicken anti-Tbr2 (Millipore AB15894, 1:100), mouse anti-Map2 (Chemicon MAB3418, 1:300), rat anti-Ctip2 (Abcam, ab18465, 1:300), rabbit anti-Arl13b (Proteintech 17711-1-AP, 1:300), mouse anti-phospho-vimentin (MBL International D076-3S, 1:250), rabbit anti-Emx1 (Sigma HPA006421, 1:200), rabbit anti-FoxG1 (Abcam ab18259, 1:200), mouse anti-reelin, (Millipore MAB5366, 1:200), mouse anti-calretinin (Swant 6B3, 1:100), rabbit anti-Satb2 (Abcam ab34735, 1:100), rabbit anti-Otx2 (Abcam ab21990, 1:200), goat anti-En2 (Santa Cruz Biotechnology sc-8111, 1:50), goat anti-DCX (Santa Cruz Biotechnology sc-8066,1:300), mouse anti-CSPG (Abcam ab11570, 1:100), rabbit anti-Cux2 (Abcam ab130395, 1:200), mouse anti-nestin (BD G11658, 1:500), mouse anti-Pax6 (DSHB, 1:100), rabbit anti-Gsh2 (Millipore ABN162, 1:500), mouse anti-Prox1 (Chemicon MAB5654, 1:200), sheep anti-TTR (AbD Serotec AHP1837, 1:100). All antibodies have been validated for this application as evidenced by validation profile on Antibodypedia, or manufacturer's website. DAPI was added to secondary antibody to mark nuclei. Secondary antibodies labeled with Alexafluor 488, 568, or 647 (Invitrogen) were used for detection. For histological analysis, sections were stained for hematoxylin/eosin followed by dehydration in ethanol and xylene and mounting in permount mounting media. Fluorescence images were acquired on a confocal microscope (Zeiss LSM 710 or 780), and brightfield images were acquired on an EVOS microscope (Invitrogen). Quantification of fluorescence for germ layer identities in enCOR and spheroids was performed using Fiji by first setting the threshold to obtain a binary image and remove background, then the tissue was traced in the DAPI channel and mean gray value measured for all channels. Fluorescence (mean gray value) was measured and calculated relative to DAPI. Quantification of brain region identities was performed by counting the number of lobules staining positive for the marker (Foxg1, Otx2, or En2) as a ratio of the total number of lobules visible by DAPI staining.

Statistical analyses. Statistical analysis of quantifications performed from imaging data was performed using Student's two-tailed t-test for significance, and the data were tested for normality by plotting a histogram of the distribution for each data set. Variance was similar between sets of data except where stated in the figure legend. Since this was the first quantitative investigation of variability in brain organoids, power calculation was not feasible due to a lack of information about population variability. Therefore, all available organoids were used for the experiments, such that the sample size for each treatment/experiment was the maximum available organoids in culture at the time. For quantifications of CP

presence and identity, samples were given IDs that masked their identity and quantifications were done blinded.

Electroporation of organoids and live imaging. Electroporation of pmax-GFP construct (Lonza) or an integrating farnesylated GFP was performed as described previously[14]. For pmax-GFP, 4 µl of 250 ng/µl were injected into several ventricular spaces followed by electroporation. The integrating farnesylated GFP (pT2-CAG-fGFP) was generated by first isolating the CAG promoter from the pCAG-GFP plasmid[35] (a gift from Connie Cepko, Addgene plasmid #11150) using FastDigest CsiI (ThermoFisher FD2114) and FastDigest BshTI (ThermoFisher FD1464) and inserting this sequence into the pT2/HB transposon donor plasmid (a gift from Perry Hackett, Addgene plasmid #26557). This plasmid was modified so that it included additional restriction sites and attR sites that would allow the insertion of sequences using Gateway cloning. To generate the farnesylated EGFP, the pENTR-EGFP2 plasmid[36] (a gift from Nathan Lawson, Addgene plasmid #22450) was linearized using EcoRI-HF (NEB R3101) and HindIII-HF (NEB R3104) and the farnesylation sequence was inserted in-frame immediately downstream of the GFP sequence. The farnesylated GFP was then cloned into the above pT2-CAG-pDest using Gateway cloning (ThermoFisher). Sleeping beauty transposase plasmid was generated by cloning the SB100X transposase (pCMV(CAT)T7-SB100 (ref. 37) was a gift from Zsuzsanna Izsvak, Addgene plasmid #34879) into the pCAGEN plasmid with CAG promoter (pCAGEN[35] was a gift from Connie Cepko, Addgene plasmid #11160). Electroporation was performed by injecting 80 ng/µl pT2-Cag-fGFP and 240 ng/µl pCAGEN-SB100X. For neuronal morphology analysis, samples were fixed 36 d after electroporation of the fGFP and analyzed by sectioning and immunohistochemistry as above.

Slice culture was performed using a modification of an *ex vivo* protocol[38]. Samples were embedded in 3% low-melting point agarose and sectioned on a vibratome to collect 300-mm sections on the air side of organotypic culture inserts (Millipore) inside a 3-cm coverglass-bottomed dish containing 1 ml serum-supplemented media: DMEM, 10% FBS, 0.5% (w/v) glucose, supplemented with penicillin-streptomycin. Sections were cultured for 1 h before changing the media to serum-free media: DMEM, 1:50 B27+A, 0.5% (w/v) glucose, glutamine, and penicillin-streptomycin. The slices were left to flatten and equilibrate overnight before imaging over several days using a Zeiss 780 and incubation chamber with 7% CO_2 at 37 °C. For this long-term imaging, HEPES (25 mM final) was added for pH buffering. Tracing of neuronal migration was performed using the Fiji plug-in MTrackJ.

Calcium imaging was performed as previously described[14] using Fluo-4 Direct (Life Technologies) on slice cultures. Frames were analyzed in ImageJ and progressive increasing intensity was corrected by using the Bleach Correction function on frames in reverse order. Individual cell traces were performed by outlining specific cells as regions of interest and mean gray value measured. $\Delta F/F$ was calculated as follows: (mean gray value – minimum gray value)/minimum gray value.

RT-PCR analysis of gene expression. Three organoids for each condition were collected in Trizol reagent (Thermo Fisher) and RNA isolated according to manufacturer. DNA was removed using DNA-Free kit (Ambion) and reverse-strand cDNA synthesis was performed using Superscript III (Invitrogen). PCR was performed using primers for a panel of pluripotent and germ layer identities (R&D systems, SC012).

RNA-seq analysis. Three individual H9 organoids for each condition were collected at the indicated time points. RNA was isolated using Arcturus PicoPure RNA Isolation Kit (Thermo Fisher Scientific, cat. #KIT0204) (20 d time point) or Trizol Reagent (Thermo Fisher Scientific, cat. #15596018) (60 d time point) according to the manufacturer's instructions. RNA concentration and integrity was analyzed using RNA 6000 Nano Chip (Agilent Technologies, cat. #5067-1511). RNA was enriched for mRNA using Dynabeads mRNA Purification Kit (Thermo Fisher Scientific, cat. #61006). Libraries were prepared using NEBNext Ultra Directional RNA Library Prep Kit for Illumina (NEB, cat. # E7420L). Barcoded samples were multiplexed and sequenced 50 bp single-end on a

HighSeq2500 (Illumina). Sample preparation and sequencing was performed at the VBCF NGS Unit (http://www.vbcf.ac.at).

The strand-specific reads were screened for ribosomal RNA by aligning with BWA (v0.6.1)[39] against known rRNA sequences (RefSeq). The rRNA subtracted reads were aligned with TopHat (v1.4.1)[40] against the *Homo sapiens* genome (hg38) and a maximum of six mismatches. Maximum multi-hits was set to 1 and InDels as well as Microexon-search was enabled. Additionally, a gene model was provided as GTF (UCSC, 2015_01, hg38). rRNA loci were masked on the genome for downstream analysis. Aligned reads were subjected to fragments per kilobase of transcript per million (FPKM) estimation with Cufflinks (v1.3.0)[41,42]. In this step bias detection and correction was performed. Furthermore, only those fragments compatible with UCSC Ref-seq annotation (hg38) of genes with at least one protein-coding transcript were allowed and counted toward the number of mapped hits used in the FPKM denominator. Furthermore, the aligned reads were counted with HTSeq (0.6.1p1) and the genes were subjected to differential expression analysis with DESeq2 (v1.6.3)[43].

GO term enrichment analysis was performed on genes with an adjusted *P* value <0.1 and absolute log2fc value >1 in at least one of the conditions (20-d or 60-d spheroid or enCOR). Each set of differentially expressed genes were analyzed using Pantherdb.org for GO Slim biological process enrichment and fold enrichment for terms as well as multi-test corrected *P*-value (plotted as $-\log_{10}(P\text{-value})$) (**Supplementary Table 1**).

For hierarchical cluster analysis, genes were sorted based on their similarity of log2fc values by means of Ward hierarchical clustering using heatmap.2 of the gplots package in R. Cutree function gave the seven clusters used for subsequent GO term analysis. Gene lists were fed into Pantherdb.org for GO Biological Process Complete, yielding a large list of redundant terms. Therefore, in order to remove redundancy, we narrowed the list using GO Trimming and a cutoff of terms with fold enrichment value >2 yielding the list of GO terms that were plotted by fold-enrichment value and $-\log_{10}(P\text{-value})$ (**Supplementary Table 2**). Individual tracks were visualized using Integrative Genomics Viewer IGV_2.3.68 (Broad Institute).

For comparison to Allen BrainSpan human transcriptome data set, the RPKM expression values of Brainspan were downloaded (http://www.brainspan.org/static/download.html). FPKM values were filtered for differential expression in the 60-d time-points (padj < 0.1) and joined with Brainspan via the gene symbols. The similarity of expression was compared by the rank of the expressed gene via Spearman correlation. The heatmap of Spearman coefficient for each region at fetal time points was generated using heatmap.2 without hierarchical clustering. The list was manually ordered according to anterior-posterior regional position and separated into four developmental stages.

34. Otani, T., Marchetto, M.C., Gage, F.H., Simons, B.D. & Livesey, F.J. 2D and 3D stem cell models of primate cortical development identify species-specific differences in progenitor behavior contributing to brain size. *Cell Stem Cell* **18**, 467–480 (2016).
35. Matsuda, T. & Cepko, C.L. Electroporation and RNA interference in the rodent retina *in vivo* and *in vitro. Proc. Natl. Acad. Sci. USA* **101**, 16–22 (2004).
36. Villefranc, J.A., Amigo, J. & Lawson, N.D. Gateway compatible vectors for analysis of gene function in the zebrafish. *Dev. Dyn.* **236**, 3077–3087 (2007).
37. Mátés, L. *et al.* Molecular evolution of a novel hyperactive Sleeping Beauty transposase enables robust stable gene transfer in vertebrates. *Nat. Genet.* **41**, 753–761 (2009).
38. Daza, R.A.M., Englund, C. & Hevner, R.F. Organotypic slice culture of embryonic brain tissue. *CSH Protoc.* **2007**, t4914 (2007).
39. Li, H. & Durbin, R. Fast and accurate short read alignment with Burrows-Wheeler transform. *Bioinformatics* **25**, 1754–1760 (2009).
40. Trapnell, C., Pachter, L. & Salzberg, S.L. TopHat: discovering splice junctions with RNA-Seq. *Bioinformatics* **25**, 1105–1111 (2009).
41. Trapnell, C. *et al.* Transcript assembly and quantification by RNA-Seq reveals unannotated transcripts and isoform switching during cell differentiation. *Nat. Biotechnol.* **28**, 511–515 (2010).
42. Roberts, A., Trapnell, C., Donaghey, J., Rinn, J.L. & Pachter, L. Improving RNA-Seq expression estimates by correcting for fragment bias. *Genome Biol.* **12**, R22 (2011).
43. Love, M.I., Huber, W. & Anders, S. Moderated estimation of fold change and dispersion for RNA-seq data with DESeq2. *Genome Biol.* **15**, 550 (2014).